



# CHORUS

This is the accepted manuscript made available via CHORUS. The article has been published as:

## Electric microfields in dense carbon-hydrogen plasmas

Stefan Hau-Riege and Jon Weisheit

Phys. Rev. E **91**, 033106 — Published 11 March 2015

DOI: [10.1103/PhysRevE.91.033106](https://doi.org/10.1103/PhysRevE.91.033106)

# Electric Microfields in Dense Carbon/Hydrogen Plasmas

Stefan Hau-Riege<sup>a</sup> and Jon Weisheit<sup>b</sup>

<sup>a</sup>Lawrence Livermore National Laboratory, Livermore, CA 94550

<sup>b</sup>Department of Physics & Astronomy, University of Pittsburgh, Pittsburgh, PA 15260

## Abstract:

*Classical molecular dynamics is used to investigate stationary and time-dependent properties of microfields in hot, solid density, electron-ion plasmas. Even at the high temperatures considered here, such simulations require statistical potentials (QSPs) to mimic the essential quantum effects of diffraction and exchange symmetry for electrons. Fortunately, key results relevant to microfield distributions are found to be insensitive to different, plausible QSP choices. Atomic processes in plasmas will depend on the time-average of the microfields. It is not clear, a priori, what the time duration of this average should be. The question of how best to extract the quasi-static (low-frequency) microfield from a classical MD simulation is explored in some detail, and the time-averaging approach we adopt involves both plasma and atomic timescale constraints. One of the major discoveries described in the paper is that for a large time interval, the time-averaged microfield does not significantly change. Our discussion of this first published suite of large simulations for plasma mixtures focuses on understanding various features and trends revealed by data for C/H plasmas having carbon fractions ranging from 0.01 to 1, and different temperatures well above  $T_{\text{Fermi}}$ .*

## I. Introduction

Fluctuations in a plasma's charge and current densities give rise to local electromagnetic fields. Equilibrium averages of these fields over macroscopic volumes and/or long times are negligible, but on atomic scales local field strengths can be sufficient to affect various elementary processes. The most important and best studied of these phenomena is Stark broadening of spectral lines, caused by the stochastic electric microfield  $\mathbf{F}(\mathbf{r},t)$  experienced by individual, radiating atoms/ions in a plasma [1,2]. The characteristic strength of these localized fields varies roughly as (density)<sup>2/3</sup>, so a thorough understanding of electric microfields remains essential for the quantitative spectroscopy of dense plasmas [3]. Magnetic microfields  $\mathbf{B}(\mathbf{r},t)$ , having strengths under thermal conditions of order  $B/F \sim \sqrt{T/m_e c^2}$ , where  $T$  is the plasma temperature in energy units, tend not to be important unless a plasma is driven to a highly non-equilibrium state [4,5].

During the past few decades, evolving experimental capabilities have enabled studies of matter of increasingly complex composition and under ever more extreme conditions. Of particular importance are novel high-power laser facilities such as the

National Ignition Facility (NIF) [6] and the Orion Laser [7], as well as x-ray free-electron lasers like the Linac Coherent Light Source (LCLS) which feature an unprecedented peak brightness that is a factor of more than  $10^9$  larger than third-generation synchrotrons [8]. In the field of plasma modeling, noteworthy additions to the computational capabilities for spectroscopy research include the APEX microfield method [9,10], and classical molecular dynamics (MD) simulations of non-ideal plasmas [11]. The former is now a well-established prescription [12], while the latter is still a developing research area. Recent surveys and conference proceedings [13-15] highlight several interesting MD investigations relevant to microfields [e.g., 16-19]. However, the limited scope and modest computational size typical of these simulations limit their ability to reveal trends involving different plasma conditions, or to obtain reliable information about statistically improbable parameter regimes. Ongoing developments in simulation science make such constraints no longer inevitable.

For this work we have used a version of the massively parallel classical MD code *ddcMD* which, when executed on large computer platforms, can efficiently track millions of particles for millions of time steps [20,21]. As the centerpiece of Lawrence Livermore's Cimarron Project, *ddcMD* already has been used in several comprehensive studies of high energy density plasma phenomena [21-26]. This paper describes our first investigation of electric microfields, using simulations that have  $1.5 \times 10^5$  to  $2.1 \times 10^6$  particles, and timesteps  $\Delta t \leq 10^{-19}$  sec. After the plasma had been equilibrated, the microfields were recorded periodically to calculate time-correlation functions. Time-averaged microfields were calculated by accumulating the microfields at every timestep inside the simulation code.

We focus on solid density, fully ionized C/H mixtures. One key motivation for investigating such mixtures is the continued use of line radiation from high-Z "dopants" to diagnose conditions in dense, laser-produced targets [27-29]. A second is to develop the foundation for a forthcoming study of the APEX model, as it is applied to multi-element plasmas [10,12].

A classical system of ions and electrons interacting through Coulomb forces tends to collapse. To avoid this unphysical behavior, Monte Carlo calculations of dense plasma properties have been based on *ion-only schemes* -- the one-component plasma (OCP) model [30] of unscreened ions embedded in a uniform electron fluid, or a model of ions interacting via Yukawa potentials that represent the static electron screening of a polarized electron fluid [31]. The ion-only approach also was used in some early MD studies of microfields in high-density plasmas [e.g., 32,33]. A major advance was the introduction of so-called quantum statistical potentials (QSPs) to classical MD simulations of high-temperature plasmas containing both electrons and ions. These potentials, which "regularize" the Coulomb interaction at short range, originally were devised to mimic quantum effects in the calculation of *stationary*, configurational properties of classical Coulomb systems [as discussed by, e.g., 34], but Hansen and collaborators [35-37] extended the use of QSPs to the time-dependent domain. The main advantage thereby gained is that one can study consequences of correlations

among *all* the charges in a system – something not possible in ion-only approaches – and, with MD, to follow the time evolution of these effects.

Although virtually all classical electron-ion MD simulations now use some version of QSPs, concerns persist about unintended and perhaps unphysical consequences of doing so (see, e.g., [21-26]). Therefore, in Sec. II we focus on this frequently ignored issue and investigate the sensitivity of particle and microfield probability distributions, and microfield autocorrelation functions, to various QSPs. We found that for the physical regimes considered in this paper, the choice of QSP does not affect the short-time-averaged microfield distribution that is relevant for atomic processes in a plasma. Of course, quantum molecular dynamics (QMD) methods avoid the need for QSPs by describing the electrons via (quantum) density functional methods [34]. However, in QMD only the ions actually are treated dynamically, using a Born-Oppenheimer scheme that – time-step by time-step – determines just the *stationary (equilibrium)* electron density for the extant configuration of ions. Because QMD time-steps are set by ion motions, this more rigorous approach is incapable of investigating the faster dynamical electron effects of relevance here.

In Sec. III we turn our attention to different prescriptions for extracting the quasi-stationary, “slow” microfield distribution from the more rapidly evolving distribution of total field strengths. Because only the slow component contributes to the quasi-static Stark splitting of atomic states, this separation must be carried out before electron-ion MD results can make direct contact with traditional line broadening methods. We found that, within limits that we identify, the slow microfield depends only weakly on the averaging time, which is a great benefit for modeling atomic processes influenced by dense plasma microfields. For simplicity, the computations of these two sections are restricted to pure carbon plasmas.

In Sec. IV, we present and discuss simulation results for microfield distributions in several carbon/hydrogen plasmas of varying composition and temperature. Here, each ion species  $\alpha$  has a specified charge, mass, and number of particles, denoted by  $\{Z_\alpha, M_\alpha, N_\alpha\}$ , and mean density  $n_\alpha = N_\alpha / \Omega$ , where  $\Omega$  is the system volume. The mean electron density,  $n_e = N_e / \Omega = \sum Z_\alpha N_\alpha / \Omega = \left(\sum Z_\alpha \xi_\alpha\right) N_{ion} / \Omega = \bar{Z} n_{ion}$ , is fixed by charge neutrality, with  $\xi_\alpha = N_\alpha / N_{ion}$  being the  $\alpha$  species’ relative concentration. The present simulations have fractional carbon abundances of  $0.01 \leq \xi_C \leq 1$ , and a range of temperatures well above the degeneracy limit given by  $T_{Fermi} = \hbar^2 (3\pi^2 n_e)^{2/3} / 2m_e$ .

Finally, in Sec. V, we collect our principal findings.

## II. Microfield Sensitivity to QSPs

For a homogeneous and isotropic system, ensemble-averaged local densities  $n_\kappa(\mathbf{r})$  of various species  $\kappa = (e, \{\alpha\})$  surrounding a given charge of species  $\mu$  are

functions only of the scalar distance  $r$ , and can be specified in terms of pair distribution functions, viz.,  $g_{\mu\kappa}(r) = n_{\kappa}(r) / n_{\kappa}$ . These distributions represent the configurational averages of the separations of just the  $\mu$ - and  $\kappa$ -particle pairs [38], viz.,

$$g_{\mu\kappa}(r) = \frac{\Omega}{N_{\mu}N_{\kappa}} \left\langle \sum_{i=1}^{N_{\mu}} \sum'_{j=1}^{N_{\kappa}} \delta(\mathbf{r} + \mathbf{r}_{\mu i} - \mathbf{r}_{\kappa j}) \right\rangle, \quad (1)$$

and knowledge of them enables one to compute corrections to ideal gas results for a system's thermodynamic functions. In Eqn. (1)  $\mathbf{r}_{\mu i}$  denotes the location of the  $i^{\text{th}}$  particle of species  $\mu$ , and the prime on the second sum means that the term  $j=i$  is to be omitted if  $\kappa = \mu$ . The averaging process itself involves pair interaction energies  $\{u_{ee}(r), u_{e\alpha}(r), \text{etc}\}$  of all species; for point charges these energies are pairwise additive. Further, in the thermodynamic limit one has  $g_{\mu\kappa}(r) = g_{\kappa\mu}(r)$ , and for all practical purposes this equality is reproduced by our large simulations.

The distribution  $W(\mathbf{F}[\mathbf{r}_1])$  of vector fields that a given particle "1" experiences likewise depends on a configurational average involving other particle positions, and because of homogeneity and isotropy its relation to the distribution  $P(F)$  of scalar field strengths is

$$P(F) = 4\pi F^2 W(\mathbf{F}[\mathbf{r}_1]) = 4\pi F^2 \left\langle \delta\left(\sum_{i \neq 1} \mathbf{f}_{i1} - \mathbf{F}[\mathbf{r}_1]\right) \right\rangle, \quad (2)$$

where the summation represents contributions  $\mathbf{f}_{i1}$  to the total field  $\mathbf{F}[\mathbf{r}_1]$  of all other particles, for a particular set of separations  $\{r_{i1} = |\mathbf{r}_1 - \mathbf{r}_i|\}$ . There is enough similarity of form between Eqs. (1) and (2) to suggest that the sensitivity of the  $\{g_{\mu\kappa}\}$  to different QSPs will be indicative of how much QSPs influence various species' microfield distributions.

To demonstrate this connection, we used the hypernetted chain (HNC) approximation [38] with different QSPs to compute the three pair distributions in fully ionized carbon plasmas; many studies have established the good agreement between such HNC results and the distributions extracted from MD. Our reference potentials are those adopted by Hansen and collaborators [38]:

$$u_{ee}^S(r) = T(\ln 2) \exp\left\{- (4\pi r^2) / [(\ln 2)\Lambda_{ee}^2]\right\}, \quad (3)$$

$$u_{\kappa\mu}^{DB}(r) = (Z_{\kappa}Z_{\mu}e^2 / r) \left[1 - \exp(-2\pi r / \Lambda_{\kappa\mu})\right], \quad (4)$$

where  $\Lambda_{\kappa\mu} = \sqrt{2\pi\hbar^2 / M_{\kappa\mu}T}$  is the thermal de Broglie wavelength of a particle whose mass  $M_{\kappa\mu}$  is the reduced mass of the pair  $(\kappa, \mu)$ . These expressions originally were developed

to incorporate separate quantum phenomena in a classical Boltzmann factor that approximates the two-body Slater sum in a system's configuration integral: Superscript S identifies that part of the QSP representing the effect of (anti)symmetry on the  $(e,e)$  interaction in an unpolarized gas [39,40], and superscript DB, the part representing regularization of the Coulomb term by diffractive smearing, in the form derived by Dunn and Broyles [41].

The given form of  $u^S$  is fairly standard (with simulations either including it, or not), but there are two other diffractive QSPs frequently used in classical MD. One, the potential of Kelbg [42],

$$u_{\kappa\mu}^K(r) = (Z_\kappa Z_\mu e^2 / r) \left[ 1 - \exp(-4\pi r^2 / \Lambda_{\kappa\mu}^2) + (2\pi r / \Lambda_{\kappa\mu}) \operatorname{erfc}(2\sqrt{\pi} r / \Lambda_{\kappa\mu}) \right], \quad (5)$$

is obtained from a perturbative solution of the two-particle Bloch equation. Numerically,  $u^K$  is similar enough to  $u^{DB}$  [43] that we do not include it in the comparisons that follow. The other, introduced and employed by Calisti, Talin, and collaborators [44,45], is phenomenological and constructed to improve the modeling of atomic ionization/recombination energetics in MD simulations. For an ionic core of charge  $Ze$  one defines a regularization length  $\delta_z$  such that  $Ze^2 / \delta_z$  equals the energy of binding of an electron to that core, and then sets the  $(e,Z)$  QSP to be

$$u_{eZ}^{CT}(r) = (-Ze^2 / r) [1 - \exp(-r / \delta_z)]. \quad (6)$$

With this choice, there is no dependence on plasma parameters, and no regularization of the interaction between charges of like sign. At high temperature  $\delta_z$  can be substantially larger than  $\Lambda_{eZ}$  (the difference growing with increasing temperature), in which case this modified Coulomb attraction is much weaker than that specified by either Eqn. (4) or (5).

Figure 1 displays HNC pair distribution functions in a fully ionized carbon plasma ( $\xi_c = 1$ ) for various QSP choices. The conditions are  $T=200eV$  and approximately normal C solid density,  $n_c = 10^{23} / cm^3$ , so the typical distance between carbon nuclei is  $(3 / 4\pi n_c)^{1/3} = 2.53a_0$ . The first panel (1a) shows all three distributions,  $g_{ee}(r)$ ,  $g_{eC}(r)$ , and  $g_{CC}(r)$ , as determined by our reference choice, “DB+S”, Eqs. (4) and (3); each of the other panels shows one these three pair distributions, but computed from the coupled HNC equations with different QSPs. Consider, first, the distribution of  $C^{+6}$  pairs. On the scale of these curves, diffractive softening of the Coulomb interaction has no discernible effect on  $g_{CC}(r)$ , and neither does the inclusion of the  $(e,e)$  symmetry interaction  $u^S$ . In contrast, the plotted  $(e,e)$  pair distributions show sensitivity both to diffractive softening (DB vs. CT) and to the symmetry interaction (DB+S vs. DB). The largest difference, by far, involves the  $g_{eC}(r)$  curves corresponding to alternative

regularizations of the  $(e, C^{+6})$  interaction (CT). Under the specified conditions, the difference between small- $r$  screening lengths is considerable,  $\delta_c = 0.33a_0$  vs.

$\Lambda_{eC} / 2\pi = 0.15a_0$ , and the consequent, twice greater depth of  $u^{DB}$  vis-à-vis  $u^{CT}$  leads to an order-of-magnitude electron density enhancement near each nucleus.

Since temperature is the lone QSP variable for hot and dense (but non-degenerate) systems, statements in the above paragraph also apply, at least qualitatively, to the plasma conditions and compositions we will study in Sec. IV. We decided, therefore, that our  $P(F)$  sensitivity studies could be limited to just three QSP choices: CT, DB, and DB+S. Comparisons involving the first two of these three highlight differences arising just from alternative regularizations of the Coulomb interactions; those involving the last two, just the influence of quantum symmetry constraints on  $(e, e)$  pairs; and those involving the first and third, the combined effects of all plausible QSP differences – (1) regularization, or not, of the  $(e, e)$  and  $(ion, ion)$  Coulomb interactions; (2) inclusion, or not, of the  $(e, e)$  symmetry constraint; and (3) the alternative approaches to regularizing the  $(e, ion)$  interaction.

In Figure 2a we have plotted the distribution of scaled microfields,  $P(\beta) = P(F / F_0) = F_0 P(F)$ , experienced by  $C^{+6}$  ions in a plasma with the same conditions as given above; here and everywhere below, fields are measured in atomic units, viz.,  $\beta = F / F_0$ , with  $F_0 = e / a_0^2 = 27.2 \text{ Volt} / a_0$ . These are the total field strengths computed by our MD code, with contributions from all particles. The different regularizations of the Coulomb interaction, as defined in Eqs. (4) and (6), clearly have a large effect. In particular, the probability of high fields at  $C^{+6}$  ions is much reduced by the weaker  $(e, C^{+6})$  attraction afforded by  $u^{CT}$ . On the other hand, the influence of the  $(e, e)$  symmetry constraint on the total field distribution at carbon ions is minimal. In Figure 2b we see that in this plasma the total field distribution at electrons is insensitive to the different QSP choices we considered.

Complementary, time-dependent microfield information is contained in the field's autocorrelation function [19,46,47],

$$A(t) = \langle \mathbf{F}(t) \cdot \mathbf{F}(0) \rangle / \langle \mathbf{F}(0) \cdot \mathbf{F}(0) \rangle. \quad (7)$$

Dominant features of  $A(t)$  can be expected near the timescale of collective motions by electrons,  $t_e = 1 / \omega_e$ , where  $\omega_e$  is the usual electron plasma frequency, and near the corresponding ion timescale,  $t_{ion} = 1 / \omega_{ion}$ , where for a mixture

$$\omega_{ion} = \left( \sum_{\alpha} \omega_{\alpha}^2 \right)^{1/2} = \omega_e \left[ \sum_{\alpha} \left( \xi_{\alpha} Z_{\alpha}^2 m_e / \bar{Z} M_{\alpha} \right) \right]^{1/2}. \quad (8)$$

In Figure 2c we show this normalized quantity  $A(t)$  for fields at  $C^{+6}$ , determined by data from separate, but otherwise equivalent, simulations with the three different

QSP choices. At all times, the autocorrelations found with and without the  $(e,e)$  symmetry interaction (DB+S and DB) are essentially the same. That the CT curve exhibits somewhat slower de-correlation at early times can be explained as follows: Relative to that of CT, the DB Coulomb regularization yields more electrons close to each nucleus, as indicated by the curves for  $g_{ec}(r)$ . Not only are these additional nearby electrons producing stronger total fields  $\mathbf{F}$ , as shown in Fig. 2a, but also their individual contributions to  $\mathbf{F}$  are changing faster because of their enhanced proximity. Taken together, these facts lead to quicker de-correlation in the DB cases. However, for all three QSPs the prompt electron de-correlation is complete within the timescale  $t_e = 0.023 fs$ . Following that, there is a time interval of order many  $t_e$  during which the total field's autocorrelation function exhibits a plateau and changes very little. Only much later, when  $t \approx t_c = 1/\omega_c = 1.4 fs$  and ionic de-correlation is complete, is there a merging of curves representing different regularizations of the  $(e,ion)$  Coulomb interaction (DB or CT). Similar comments apply to autocorrelations we obtained from MD simulations of the C/H plasma mixtures described in Sec. IV.

### III. Extraction of the Slow Microfield Component

The distribution of strengths of the total microfield due to each of a plasma's constituent species is straightforward to determine from an MD simulation. However, as noted in the introductory remarks, this is not the quantity relevant to traditional line-broadening calculations. Such work treats rapidly changing Stark perturbations as collisions that alter the wave train of a radiating ion, and slowly changing Stark perturbations as the cause of a quasi-static splitting of the radiator's levels [see again, 1,2]. The fast/slow microfield division – into what often is referred to as its high-frequency and low-frequency components – unfortunately is not just a matter of identifying the electrons' and the ions' contributions to the distribution of the total field  $\mathbf{F}$  at an ion of interest. As emphasized by Baranger and Mozer [48], some part of the electrons' microfield must be subtracted from the high-frequency component and included with the low-frequency one, because each perturbing ion carries with it a quasi-static shielding cloud composed of an ever-changing group of electrons. The Coulomb coupling parameter  $\Gamma_{ez} = Ze^2 / a_z T$ , with the ion sphere radius  $a_z$  being defined by  $4\pi a_z^3 n_e / 3 = Z$ , is a measure of the efficacy of this shielding and, therefore, of the importance of the subtraction process. Although the complicating effects of any bound electronic states (whose existence is necessary to spectroscopy) are not considered in the simulations, we note that these states seldom occur for ions when conditions are such that  $\Gamma_{ez}$  exceeds unity [49].

In a version of the one-component plasma (OCP) model, mobile electrons are completely uncoupled from a uniform background charge density representing the ions, and hence  $\Gamma_{ez} = 0$ . In this model, the computed microfield is that of the electrons only and perforce it approximates the high-frequency component. The Holtmark distribution represents the OCP's limiting case of uncorrelated electrons. On the other

hand, if every “particle” in a system corresponds to an ion shielded by a fixed electron screening cloud, the computed microfield approximates just the low-frequency component. The weak coupling (small  $\Gamma_{eZ}$ ) Yukawa screening models of Baranger and Mozer [48], of Hooper [50], and APEX [9,10,12], are in this category.

Dufty [51] used time dependent properties of a plasma’s charge density fluctuations to formally separate the electrons’ dynamic, “collisional” effects from the static, (ion) “Stark” effects on a spectral line profile, but as yet there are no explicit calculations based on his final expressions. More recently, Nersisyan *et al* [52] published the PMFEX microfield method. It allows one to drop the constraint of fixed, Yukawa screening and to calculate equilibrium contributions to the *total* microfield from both electron and ions, using potentials of mean force,  $u_{ku}^{MF}(r) = -T \ln[g_{ku}(r)]$ . However, as it stands, this approach is not useful for spectroscopy because there is no way to carry out the requisite short-time averaging of the total field.

Multi-component MD simulations do not involve such issues, and therefore offer the ability to test directly the accuracy and limitations of various microfield models. Within the past decade, Calisti and colleagues [19,44] have carried out MD simulations to obtain time-dependent microfields in hydrogen plasmas, using a straightforward definition of the slow and fast fields that a radiator is experiencing at time  $t$ . We adopted their concept, but use an integral that involves only past times,  $t' \leq t$ ,

$$\mathbf{F}_{slow}^{[\tau]}(t) = \frac{1}{\tau} \int_{t-\tau}^t \mathbf{F}(t') dt', \quad \text{and} \quad \mathbf{F}_{fast}^{[\tau]}(t) = \mathbf{F}(t) - \mathbf{F}_{slow}^{[\tau]}(t). \quad (9)$$

These authors argued that a good choice for the averaging interval  $\tau$  would yield only a weak correlation between the ion component of  $\mathbf{F}$  (which dominates  $\mathbf{F}_{slow}$ ) and the remaining, electron component (which dominates  $\mathbf{F}_{fast}$ ), and they expected  $\tau$  to lie between the proton and the electron response times,  $t_H = 1/\omega_H$  and  $t_e = 1/\omega_e$ . Unfortunately, their simulations for a system with  $\Gamma_{eH} = 0.2$  showed only a gradual and ongoing de-correlation of  $\mathbf{F}_e$  and  $\mathbf{F}_{ion}$  throughout that interval, and left unanswered the question: what is the best choice of averaging interval  $\tau$ ? (Of course, the correlation of these fields goes to zero eventually because, over macroscopic times, thermal microfields produce no net forces.)

To explore the averaging issue further, we first used the reference QSPs (DB+S) to compute distributions of  $F_{slow}^{[\tau]}$  experienced by  $C^{+6}$  ions in a solid density carbon plasma, for a wide range of  $\tau$ -values and for three temperatures,  $T = 83, 200, \text{ and } 830\text{eV}$  (corresponding to  $\Gamma_{eC} = 0.78, 0.32, 0.08$ ). These simulation results are displayed in the panels of Figure 3. Readily apparent at all temperatures is a decrease in the mean strength of the slow field with increasing interval  $\tau$ , as more and more of the fluctuating (vector) field is averaged out. Also evident is the trend that, as  $T$  increases and electrons become less localized near the ions, it takes longer for strong fields, due mostly to

electrons, to be diminished by time averaging. It is possible for both of these results to be anticipated on the basis of comments pertaining to Fig. 2. But, what is unexpected is the  $F_{slow}^{[\tau]}$  “ $\tau$  plateau” – the limited range of  $\tau$ -values over which there is little change in the  $F_{slow}^{[\tau]}$  distribution – suggesting completion of the  $\mathbf{F}_{fast} / \mathbf{F}_{slow}$  separation. Here, this plateau occurs between about 0.2 and 0.6 fs, well within the interval  $(t_e, t_c)$ .

According to the autocorrelation data plotted in Figure 4a, at each temperature the  $\tau$  plateau of  $F_{slow}^{[\tau]}$  distributions is located near the end of the temporal plateau exhibited by  $A(t)$ . Our efforts to improve on just a visual estimate of an optimal  $\tau$ -value, in the sense that small deviations about this value result in minimal overall changes to  $P(F_{slow}^{[\tau]} / F_0)$ , led us to devise a “gradient of the distribution” metric. For two distributions, constructed from fields having tau-values  $\tau_1$  and  $\tau_2$ , the gradient is defined as  $\|P(F_{slow}^{[\tau_1]} / F_0) - P(F_{slow}^{[\tau_2]} / F_0)\|_2 / |\log(\tau_1) - \log(\tau_2)|$ , where  $\|\dots\|_2$  indicates the L2 norm. The distribution gradient is shown in Fig. 4b. For smaller  $\tau$ -values, the microfield distribution is changing rapidly, leading to large gradient values. For larger  $\tau$ -values, the distributions change less and, in this case, the gradient exhibits a minimum at  $\tau$ -values around 0.5 to 1.0 fs; this coincides with the end of the temporal plateau exhibited by  $A(t)$ .

Without a substantial set of  $F_{slow}^{[\tau]}$  distributions, and/or specific total field autocorrelation function information, some estimate of the optimal averaging interval is needed if  $F_{slow}$  is to be determined via Eq. (9). The general constraint  $t_e < \tau < t_{ion}$  is not sufficient to this end. The optimal interval also must satisfy certain atomic criteria because bound states are involved when  $F_{slow}^{[\tau]}$  is employed to determine Stark shifts for spectroscopy [3]. Specifically:

- (i) Let  $t_{orb}(Z, n)$  be the Bohr orbital period of an electron bound to an ionic core of charge  $Z$  and having principal quantum number  $n$ ; then,  $t_{orb}(Z, n) < \tau$  is needed to insure that this level retains stationary properties in the presence of temporal  $F_{slow}$  variations. [53].
- (ii) Let  $\Delta E = \hbar\Delta\omega$  be the unperturbed energy of transition between two extant levels in a plasma ion of spectroscopic interest (a “radiator”); then,  $\tau \Delta\omega > 1$  is needed to insure that the Stark effect these levels experience due to  $F_{slow}$  is quasi-static.

Both inequalities can be quantified once the concept of plasma continuum lowering is introduced. In brief, continuum lowering (CL) represents the leading order of a plasma’s “environmental impact” on the bound states of its embedded ions – charges surrounding a radiator produce an electrostatic potential that is roughly constant over atomic dimensions, and this potential effectively reduces binding energies (i.e., lowers the continuum). The simplest CL picture is one of pressure ionization, whereby the only levels remaining have Bohr orbits contained within the ion sphere [54]. This

gives a density -- but not temperature -- dependence to the uppermost bound level, i.e.,  $n_{\max}^2 = (Za_z / a_0)$ , and, hence, to the constraint involving the orbital period,

$$\tau > t_{orb}(Z, n_{\max}) = (2\pi n_{\max}^3 / Z^2)(a_0 / \alpha c) = (2\pi\sqrt{3})t_e. \quad (10)$$

By setting the minimum frequency difference to be that between levels  $n_{\max}$  and  $n_{\max} - 1$ , and then using the same expression for the uppermost level in the presence of pressure ionization, the second of the above constraints becomes

$$\tau > \frac{1}{\Delta\omega[(Z, n_{\max}), (Z, n_{\max} - 1)]} \approx \frac{t_{orb}(Z, n_{\max})}{2\pi} = t_e\sqrt{3}. \quad (11)$$

The similarity of these two results, and the fact that more realistic CL theories tend to yield greater lowering of the continuum (viz., smaller values of  $n_{\max}$ ) [24], together indicate that  $\tau > t_{atom} = 10t_e$  represents a conservative constraint due to atomic phenomena.

Unless other criteria are available we recommend the geometric mean expression,

$$\tau^* = \sqrt{t_{atom}t_{ion}} \geq 20t_e, \quad (12)$$

for estimating of the optimal averaging interval. It always gives a  $\tau$ -value in harmony with the above constraints, and its value for the solid density carbon plasma,  $\tau^* = 0.56 fs$ , agrees with the results plotted in Fig. 4. It should be noted, though, that this formula does not contain any temperature dependence, such as is suggested by the curves in Fig. 4b. And, it should be recognized that use of the microfield  $F_{slow}^{[\tau]}$ , with any  $\tau < t_{ion}$ , excludes the so-called ‘‘ion dynamics’’ [13] – the broadening effect of *perturber* ions’ motions on the cores of spectral lineshapes.

We also looked at two numerical schemes, based solely on information available at a simulation’s current time-step, which might provide accurate distributions of  $F_{slow}$ . In one of these, whose fields we label  $F_{slow}^{[e]}$ , we subtract from the  $\mathbf{F}$  at each  $C^{+6}$  ion the fields of all electrons currently within its ion sphere; in some sense, these electrons are ‘‘in collision’’ with the central  $C^{+6}$ . In the other, whose fields we label  $F_{slow}^{[all]}$ , we subtract from  $\mathbf{F}$  the fields of *all* other charges currently within that sphere. Field strength distributions for both of these simple models are compared in Fig. 5 with that for  $F_{slow}^{[\tau]}$ , with  $\tau = 0.6 fs$ , for the 200 eV, solid density carbon plasma. Included in this figure is the distribution for  $F_{ion}$ , as well as the first of several distributions we obtained from MD simulations of equivalent ion-only systems involving Yukawa interactions,

$$u_{\alpha\gamma}^y(r) = (Z_\alpha Z_\gamma e^2 / r) \exp(-k_e r), \quad (13)$$

with screening due just to electrons:  $k_e = \sqrt{4\pi e^2 n_e / T}$ .

Several points are apparent from the plots in Fig. 5. First, the important extent to which partial screening by electrons reduces the total ionic field  $F_{ion}$  is indicated by the difference between that field's distribution and those for the various  $F_{slow}$  alternatives. Moreover, in this case the actual (dynamic) electron screening is approximated very well by a (static) Yukawa model. However, neither of the single-time definitions,  $F_{slow}^{[e]}$  and  $F_{slow}^{[all]}$ , is particularly accurate: the former overestimates the likelihood of strong fields while the latter underestimates it. Such behavior limits their use in plasma lineshape studies, since strong fields control the prominent wings of Stark broadened lines. Still, for certain purposes one or the other of these simple pictures may suffice.

Lastly, the sensitivity of  $F_{slow}$  to different QSP choices was checked. Figure 6 shows curves for  $P(F_{slow}^{[\tau]} / F_0)$  that result when the different QSP interactions (DB+S, DB, or CT) are used in the carbon plasma simulation. Here, in sharp contrast to the curves of Figure 2a, we see very little difference among distributions. This welcome news is due, we believe, to the fact that  $F_{slow}$  is primarily a screened *ionic* field, and the distribution of ions – as represented by ion-ion pair functions  $g_{\alpha\gamma}(r)$  – is itself insensitive to the QSP alternatives.

#### IV. Microfields in Carbon/Hydrogen Mixtures

We now shift focus to properties of microfields in plasmas with more than one ion species, in order to explore composition-related issues and trends. Results described below involve the single QSP choice, DB+S, and for the most part low frequency fields are  $F_{slow}^{[\tau]}$ , with the MD's autocorrelation functions being used to determine  $\tau$ .

This large set of simulations involves fully ionized carbon/hydrogen mixtures, with the  $C^{+6}$  number fraction being  $\xi_C = 1/100, 1/3, 2/3$ , or 1, and the temperature being  $T = 83, 200$ , or  $830eV$ . In all cases, the total ion density is fixed  $n_{ion} = n_H + n_C = 1 \times 10^{23} cm^{-3}$ , so the pure carbon plasmas discussed earlier represent a subset of these conditions. There were at least  $10^4$  carbon ions in each of the simulations, and unless noted otherwise our microfield data pertain to these particles. For reference, some important plasma parameters are collected in Table 1; note that these simulations span a wide range of  $(e, C^{+6})$  coupling strengths,  $0.04 \leq \Gamma_{eC} \leq 0.78$ .

Figure 7 shows distributions of the scaled *total* field,  $P(\beta) = P(F / F_0)$ , experienced by the  $C^{+6}$  ions in C/H plasmas having various conditions: In panel 7a are curves for all four carbon fractions  $\xi_C$  at the single temperature  $T = 83eV$ , and in 7b are

curves for the same fractions, but at  $T = 830eV$ . In the lower panels are distributions of the scaled total field at carbon ions when the carbon fraction is fixed at  $\xi_C = 1/3$  (panel 7c), or at  $\xi_C = 1/100$  (panel 7d), but temperature varies. The upper panels reveal that at fixed temperature, low or high, strong total fields, i.e., those for which  $\beta = F / F_0 > 1$ , are relatively improbable when carbon is just a trace impurity,  $\xi_C = 1/100$ ; higher carbon fractions do yield greater probabilities of strong fields, but the increase of those  $P(\beta)$ -values is modest as  $\xi_C$  increases from  $1/3$  to unity. The lower panels reveal that at either of the fixed carbon fractions,  $\xi_C = 1/3$  or  $\xi_C = 1/100$ , stronger total fields are more likely when the temperature is low. To understand these trends, we note that holding T fixed while increasing  $\xi_C$  has the effect of increasing electron-ion coupling, since in this case  $\Gamma_{eC} = const \cdot [1 + 5\xi_C]^{1/3}$ . The same is true when  $\xi_C$  is held fixed and the temperature is lowered, since now  $\Gamma_{eC} = const / T$ . In both cases the increased electron-ion coupling means that each carbon ion has more close electrons, thus enabling a larger total, electron plus ion, field to occur. Lower temperatures also enhance the consequences of ion-ion repulsion, thereby lessening ionic contributions to the total field.

As before, we find that the microfield distribution trends are connected to the behavior of the pair distribution functions  $\{g_{\kappa\mu}(r)\}$  for the various plasma conditions and compositions. In the upper panels of Fig. 8 are plotted HNC results for the three pair distributions involving  $C^{+6}$  ions, for all the carbon fractions, and for  $T=200eV$ ; in the lower panels are the same pair functions, but at fixed fraction,  $\xi_C = 1/3$ , and for the temperatures  $T = 200$  and  $830eV$ . (HNC solutions for lowest temperature,  $83eV$ , did not converge). Note that the distribution of electrons about a carbon ion shows, as is expected from the comments above, a much stronger dependence on T than on  $\xi_C$ . For the repulsive ion-ion cases, pair distribution variations with T and with  $\xi_C$  are more comparable.

In the three panels of Fig. 9 we show distributions of the instantaneous total fields experienced by all three species, when carbon is a trace impurity ( $\xi_C = 1/100$ ) and has little effect on the results for electrons or protons. At the highest temperature,  $T = 830eV$  (top panel), the plasma is nearly ideal and all three distributions, being dominated by  $e$  and  $H^+$ , are essentially the same. At the intermediate temperature,  $T = 200eV$  (center panel), there is a more substantial density enhancement of electrons near the carbon ions, and this results in a tendency of  $C^{+6}$  to experience total fields somewhat stronger than those experienced by the electrons or protons; the singly charged particles, however, still exhibit identical total field distributions. At the lowest temperature (bottom panel), the carbon disparity is enhanced further. These distribution features certainly would not be unexpected for pure Coulomb systems. But, our simulations employ QSPs (DB+S) that affect the various pair interactions differently: Electron pairs also are subject to the symmetry term, Eq. (3), while proton pairs are not; plus, the Coulomb regularization, Eq. (4), is much more influential when the pair interaction involves an electron. With reference to Fig. 2, it is clear that any/all of these

QSP differences affect total field distributions in the C/H plasmas much less than the alternative regularization (CT), Eq. (6), does.

Figure 10 presents scaled distributions  $P(F_{slow}^{[\tau]} / F_0)$  for several  $\tau$ -values, at three representative  $(T, \xi_C)$  combinations (see also Fig. 3 for pure carbon plasma results). As temperature and the carbon fraction both increase in these successive panels, there clearly is a reduction in the separation of distributions (note the changing vertical axis scales). However, even at the printed scale of these plots, each case shows evidence of a plateau in the same interval as before,  $0.2 < \tau(fs) < 0.6$ . Inspection of analogous results for all the other simulated C/H conditions suggests that temperature is the more important parameter here, and this impression is supported by the “autocorrelation gradient” results plotted in Fig. 11; these curves include those shown in Fig. 4b. Additionally, the gradient plots exhibit relative minima at  $\tau$ -values somewhat higher than one would infer from the corresponding sequences of  $P(F_{slow}^{[\tau]} / F_0)$  distributions, but still close to the prediction of Eq. (12).

We have emphasized that the microfield quantity of prime interest for plasma spectroscopy is the distribution  $P(F_{slow})$ . Results from MD simulations offer the ability not only to evaluate other, less computationally demanding prescriptions for obtaining this information, but also to produce such distributions under conditions for which other methods may be unreliable or inappropriate (e.g., only MD has the potential to study systems out of thermal equilibrium). To this end, Fig. 12 presents several comparison plots. Each panel contains a set of low-frequency microfield distributions, at the location of a  $C^{+6}$  ion, for specific  $(T, \xi_C)$  conditions in dense C/H plasma: The three left panels show distributions at the fixed carbon fraction,  $\xi_C = 1/100$ , and varying temperature,  $T = 83, 200, \text{ or } 830 eV$ ; the three right panels, distributions at  $\xi_C = 2/3$  and the same three temperatures. At fixed  $\xi_C$ , the difference between the  $F_{ion}$  probability distribution and that for either the dynamically screened field  $F_{slow}^{[\tau]}$  or the static, Yukawa screened field  $F_Y$  is greater at lower temperatures. And, at fixed temperature, these differences are greater when the carbon fraction is higher. As in the discussion pertaining to Fig. 7, both trends correlate with changes in the electron-carbon coupling parameter  $\Gamma_{eC}$ , whose smaller values (see Table 1) reflect weaker screening of  $C^{+6}$ . Hence, in the plasma with the lowest carbon abundance and the highest temperature, differences among the distributions for all three of the above microfield quantities are minimal.

The close agreement, in all these simulations, between the distributions for  $F_Y$  and  $F_{slow}^{[\tau]}$  is perhaps surprising, and raises two questions. (1) Why does a simple static screening approximation so accurately mimic the true dynamical electron situation, over a wide range of conditions? (2) Why are the differences between the posited ion-ion interaction of the Yukawa scheme, Eq. (11), and the MD’s effective ion-ion interaction (the potential of mean force),  $u_{\alpha\gamma}^{MF}(r) = -T \ln g_{\alpha\gamma}(r)$ , unimportant for any of the conditions explored? The answer to the first question, we believe, is that the timescale to establish a

given ion's field  $F_{slow}^{[\tau]}$  is of order  $\tau^*$ , and in the dense plasmas of interest here this timescale is much larger than the timescale  $t_e = 1/\omega_e$  needed to establish the ion's quasi-stationary screening cloud. The answer to the second question, we believe, involves the fact that the field  $F_{slow}^{[\tau]}$  at an ion is produced mostly by distant charges ( $r > a_z$ ), as discussed in connection with Fig. 5. Therefore, for slow microfields the very different small- $r$  behaviors – divergent Yukawa potential vs. convergent potential of mean force – are of little consequence. Further, when plasma coupling is weak, the HNC theory yields potentials of mean force that have Yukawa forms at long range [38].

As part of a forthcoming, MD-based study of the APEX microfield method for multi-ionic systems, we now are performing plasma simulations that involve higher  $Z$  radiators, more complicated mixtures, and more extreme conditions. These data should prove useful also for guiding possible extensions, to plasma mixtures, of existing schemes that produce fast numerical fits for single-species Yukawa microfield distributions [31,55].

## V. Summary

In this paper we addressed, through numerous large MD simulations, the issue of how QSP choices affect the probability distributions of microfields that arise in a plasma mixture; our specific cases involved dense and fully ionized C/H of varying composition and temperature. We showed that trends observed in the microfield distributions had counterparts in related plasma pair distribution functions, and that these trends could largely be understood in terms of differing values of the electron-ion coupling parameter,  $\Gamma_{ez} = Ze^2 / a_z T$ . Next, we highlighted the question of how to compute the distribution of quasi-static (low-frequency) fields at an ion, which is essential for the standard treatment of Stark broadening of spectral lines. The best definition, we contend, involves a running time average of the total microfield at each ion over an interval  $\tau$ , whose magnitude we studied in some detail. We argued that this interval is fairly narrowly constrained. Moreover, it includes a small range of  $\tau$ -values – a  $\tau$ -plateau – for which the resulting distribution  $P(F_{slow}^{[\tau]})$  changes very little, and is not sensitive to the different QSPs we considered.

With this information in hand we then carried out a suite of simulations to explore how changing a plasma mixture's composition and/or temperature affects microfield distributions at the different charge species. In our discussion of various trends exhibited by these mixture results, we observed again the important role played by the electron-ion coupling parameter. Also, for each mixture, the  $\tau$ -plateau in its  $P(F_{slow}^{[\tau]})$  distributions was located. We noted some evidence involving both the field distributions and their autocorrelation functions that the range of optimal  $\tau$ -values is more sensitive to temperature (at fixed composition) than it is to composition (at fixed temperature); this point merits further attention. Lastly, we reported excellent

agreement between our electron-ion MD simulations and our MD simulations involving just Yukawa-screened ions, for several C/H mixtures and temperatures, and discussed likely reasons why this is so.

### **Acknowledgements**

We thank Dr. C.A. Iglesias for useful discussions, and our Cimarron colleagues for their continued interest and suggestions. This work was performed under the auspices of the U.S. Department of Energy by Lawrence Livermore National Laboratory under Contract DE-AC52-07NA27344.

## References

- [1] I.I. Sobelman, L.A. Vainshtein and E.A. Yukov, *Excitation of Atoms and Broadening of Spectral Lines* (Springer-Verlag, Berlin, 1981).
- [2] H.R. Griem, *Principles of Plasma Spectroscopy* (Cambridge University Press, Cambridge, 1997)
- [3] A.V. Demura, Intl. J. Spectrosc. **2010**, 671073 (2010).
- [4] M.Yu. Romanovsky, J. Ortner and V.V. Korobkin, Laser Physics **11**, 312 (2001).
- [5] E. Stambulchik and Y. Maron, Phys. Rev. Lett. **113**, 083002 (2014).
- [6] S.H. Glenzer, B.J. MacGowan, P. Michel, N.B. Meezan, L.J. Suter, S.N. Dixit, J.L. Kline, G.A. Kyrala, D.K. Bradley, D.A. Callahan, E.L. Dewald, L. Divol, E. Dzenitis, M.J. Edwards, A.V. Hamza, C.A. Haynam, D.E. Hinkel, D.H. Kalantar, J.D. Kilkenny, O.L. Landen, J.D. Lindl, S. LePape, J.D. Moody, A. Nikroo, T. Parham, M.B. Schneider, R.P.J. Town, P. Wegner, K. Widmann, P. Whitman, B.K.F. Young, B. Van Wonterghem, L.J. Atherton, E.I. Moses, Science **327**, 1228 (2010).
- [7] N. Hopps, C. Danson, S. Duffield, D. Egan, S. Elsmere, M. Girling, E. Harvey, D. Hillier, M. Norman, S. Parker, P. Treadwell, D. Winter, and T. Bett, Appl. Opt. **20**, 3597 (2013).
- [8] P. Emma, R. Akre, J. Arthur, R. Bionta, C. Bostedt, J. Bozek, A. Brachmann, P. Bucksbaum, R. Coffee, F.-J. Decker, Y. Ding, D. Dowell, S. Edstrom, A. Fisher, J. Frisch, S. Gilevich, J. Hastings, G. Hays, Ph. Hering, Z. Huang, R. Iverson, H. Loos, M. Messerschmidt, A. Miahnahri, S. Moeller, H.-D. Nuhn, G. Pile, D. Ratner, J. Rzepiela, D. Schultz, T. Smith, P. Stefan, H. Tompkins, J. Turner, J. Welch, W. White, J. Wu, G. Yocky and J. Galayda, Nat. Photon. **4**, 641 (2010).
- [9] C.A. Iglesias, J.L. Lebowitz and D. MacGowan, Phys. Rev A **28**, 1667 (1983).
- [10] C.A. Iglesias, H.E. DeWitt, J.L. Lebowitz, D. MacGowan, and W. B. Hubbard, Phys. Rev. A **31**, 1698 (1985).
- [11] R. Stamm and D. Voslamber, J. Quant. Spectrosc. Radiat. Transfer, **22**, 599 (1979).
- [12] C.A. Iglesias, F.J. Rogers, R. Shepherd, A. Bar-Shalom, M.S. Murillo, J. Quant. Spectrosc. Radiative Transfer **65**, 303 (2000).
- [13] S. Alexiou, High Energy Density Physics **5**, 225 (2009).

- [14] E. Stambulchik and Y. Maron, *High Energy Density Physics* **6**, 9 (2010).
- [15] A. Devdariani, editor, *Proceedings XXI International Conf. Spectral Line Shapes* ( J. Physics: Conference Series #**397**, 2012). See also the proceedings of earlier conferences in this series.
- [16] S. Sadykova and W. Ebeling, *Contrib. Plasma Physics* **47**, 659 (2007).
- [17] A. Calisti, S. Ferri, and B. Talin, *High Energy Density Physics* **5**, 307 (2009).
- [18] H.B. Nersisyan, C. Toepffer, and G. Zwicknagel, *Contrib. Plasma Physics* **50**, 193 (2010).
- [19] A. Calisti, S. Ferri, C. Mosse, B. Talin, M.A. Gigosos, and M.A. Gonzalez, *High Energy Density Physics* **7**, 197 (2011).
- [20] D.F. Richards, J.N. Glosli, B. Chan, M.R. Dorr, E.W. Draeger, J.-L. Fattebert, W.D. Krauss, T. Speice, F. H. Streitz, M.P. Surh and J.A. Gunnels, in *Proceedings of IEEE Conference on High-Performance Computing Networking, Storage and Analysis* (Portland, OR, 2009).
- [21] F.R. Graziani, V.S. Batista, L.X. Benedict, J. I. Castor, H. Chen, S.N. chen, C.A. Fichtl, J.N. Glosli, P.E. Grabowski, A.T. Graf, S.P. Hau-Riege, A.U. Hazi, S.A. Richards, H.A. Scott, R. Shepherd, L.G. Stanton, F.H. Streitz, M.P. Surh, J.C. Weisheit, and H.D. Whitley, *High Energy Density Physics* **8**, 105 (2012).
- [22] J.N. Glosli, F.R. Graziani, R.M. More, M.S. Murillo, F.H. Streitz, M.P. Surh, L.X. Benedict, S. Hau-riege, A.B. Langgdon and R.A. London, *Phys. Rev E* **78**, 205401 (2008).
- [23] R. More, F. Graziani, J. Glosli, and M. Surh, *High Energy Density Physics* **6**, 29 (2010).
- [24] S.P. Hau-Riege, J. Weisheit, J.I. Castor, R.A. London, H. Scott, and D.F. Richards, *New J Phys.* **15**, 015011 (2013).
- [25] L.X. Benedict, M.P. Surh, J.I. Castor, S.A. Khairallah, H.D. Whitley, D.F. Richards, J.N. Glosli, M.S. Murillo, C.R. Scullard, P.E. Grabowski, D. Michta, and F.R. Graziani, *Phys. Rev. E* **86**, 046406 (2012).
- [26] P.E. Grabowski, M.P. Surh, D.F. Richards, F.R. Graziani and M.S. Murillo, *Phys. Rev. Lett.* **111**, 215002 (2013).
- [27] D. Salzmann, *Atomic Physics in Hot Plasmas* (Oxford University Press, New York, 1998).

- [28] C.J. Fontes, J. Abdallah Jr, C. Bowen, R.W. Lee and Yu. Ralchenko, *High Energy Density Physics* **5**, 15 (2009).
- [29] H.A. Scott and S.B. Hansen, *High Energy Density Physics* **6**, 39 (2010).
- [30] S. Ichimaru, *Rev. Mod. Phys.* **54**, 1017 (1982).
- [31] A.Y. Potekhin, G. Chabrier and D. Gilles, *Phys. Rev. E* **65**, 036412 (2002).
- [32] E.L. Pollock and J.C. Weisheit, in *Spectral Line Shapes* **3**, F. Rostas, editor (Walter de Gruyter, Berlin, 1985).
- [33] R. Stamm, B. Talin, E.L. Pollock and C.A. Iglesias, *Phys. Rev. A* **34**, 4144 (1986).
- [34] C. S. Jones and M.S. Murillo, *High Energy Density Phys.* **3**, 379 (2007).
- [35] J.-P. Hansen and I.R. McDonald, *Phys. Rev. A* **23**, 2041 (1981).
- [36] J.-P. Hansen and I.R. McDonald, *Physics Letters* **97A**, 42 (1983).
- [37] L.Sjogren, J.-P. Hansen and E.L Pollock, *Phys. Rev. A* **24**, 1544 (1981).
- [38] J.-P. Hansen and I.R. McDonald, *Theory of Simple Liquids*, 3ed (Academic Press, London, 2006).
- [39] F. Lado, *J. Chem. Phys.* **47**, 5369 (1967).
- [40] H. Minoo, M.M. Gombert and C. Deutsch, *Phys. Rev. A* **23**, 921 (1981).
- [41] T. Dunn and A.A. Broyles, *Phys. Rev.* **157**, 156 (1957).
- [42] G. Kelbg, *Ann. Physik* **13**, 354; **14**, 394 (1964).
- [43] A.V. Filinov, M. Bonitz and W. Ebeling, *J. Phys. A: Mathematical and General* **36**, 5957 (2003).
- [44] A Calisti, B. Talin, S. Ferri, C. Mosse, V. Lisitsa, L. Bureyeva, M.A. Gigosos, M.A. Gonzalez, T. del Rio Gaztelurrutia, and J.W. Dufty, in *19<sup>th</sup> Intl. Conference on Spectral Line Shapes*, M.A. Gogosos and M.A. Gonzalez, editors (American Inst. Phys. Conf. Series, #1058, 2008).
- [45] A. Calisti and B. Talin, *Contrib. Plasma Physics* **51**, 524 (2011).
- [46] M.A. Berkovsky, J.W. Dufty, A. Calisti, R. Stamm, and B. Talin, *Phys. Rev. E* **54**, 4087 (1996).

- [47] T. Pschiwul and G. Zwicknagel. *Contrib. Plasma Physics* **41**, 271 (2001).
- [48] M. Baranger and B. Mozer, *Phys. Rev.* **115**, 521 (1959); **118**, 626 (1960).
- [49] M.S. Murillo, J. Weisheit, S.B. Hansen and M.W.C. Dharma-wardana, *Phys. Rev. E* **87**, 063113 (2013).
- [50] C.F. Hooper, Jr, *Phys. Rev.* **165**, 215 (1968).
- [51] J.W. Dufty, *Phys. Rev.* **187**, 305 (1969).
- [52] H.B. Nersisyan, C. Toepffer, and G. Zwicknagel, *Phys. Rev. E* **72**, 036403 (2005).
- [53] D.R. Bates, A.E. Kingston and R.W.P. McWhirter, *Proc. Royal Soc. (London)* **A267**, 297 (1962).
- [54] R.M. More, in *Advances in Atomic and Molecular Physics*, vol. 21, D.R. Bates and B. Bederson, editors (Academic Press, Orlando, 1984).
- [55] S. Laulan, C Blanchard and G. Faussurier, *High Energy Density Phys.* **4**, 131 (2008).

Table I. Plasma parameters for the C/H mixtures discussed in Sec. IV.

	$\xi_c = 1$	$\xi_c = 2/3$	$\xi_c = 1/3$	$\xi_c = 1/100$
$\bar{Z}$	6.0	4.3	2.7	1.0
$a_c [a_0]$	2.5	2.8	3.3	4.5
$t_e$ [fs]	0.023	0.027	0.034	0.055
83eV	0.78	0.70	0.60	0.44
$\Gamma_{ec} : 200\text{eV}$	0.32	0.29	0.25	0.18
830eV	0.08	0.07	0.06	0.04

## Captions for Figures

Figure 1. (Color online) HNC pair distribution functions in a fully ionized carbon plasma at 200 eV and  $10^{23}$  carbon atoms/cm<sup>3</sup> for various QSP choices. (a) Reference choice “DB+S”, and (b) to (d)  $g_{CC}(r)$ ,  $g_{eC}(r)$ , and  $g_{ec}(r)$  for different QSPs.

Figure 2. (Color online) Effect of the QSP on the total field probability distribution and autocorrelation function, for solid density carbon plasma at T=200 eV.

Figure 3. (Color) Slow microfield distributions at different temperatures T, for a range of averaging intervals  $\tau$ .

Figure 4. (Color online) (a) Autocorrelation and (b) distribution gradient in a carbon plasma as a function of time. These plots illustrate the very large dynamic range that the microfield simulations need to cover.

Figure 5. (Color online) Microfield distributions resulting from different schemes to approximate the slow microfield.

Figure 6. (Color online) Slow microfield distributions at C<sup>+6</sup> resulting from different QSP interactions.

Figure 7. (Color online) Distributions of the scaled *total* field  $F$  experienced by the C<sup>+6</sup> ions in C/H plasmas having various conditions.

Figure 8. (Color online) HNC calculations of the C/H pair correlation functions: (a) – (c) for fixed  $T = 200$  eV; (d) – (f) for fixed carbon abundance  $\zeta_C = 33\%$ .

Figure 9. (Color online) Distributions of the total field experienced by electrons (e), hydrogen ions (H), and carbon ions (C) at different temperatures, in C/H plasma with carbon abundance  $\zeta_C = 33\%$ .

Figure 10. (Color online) Slow microfield distributions at C<sup>+6</sup> for different temperatures and carbon abundance fractions.

Figure 11. (Color online) Distribution gradients in C/H plasma mixtures as a function of time for (a)  $T = 83$  eV, (b)  $T = 200$  eV, and (c)  $T = 830$  eV.

Figure 12. (Color online) Scaled microfield distributions at C<sup>+6</sup> ions in C/H plasmas with various temperatures T and carbon fractions  $\zeta_C$ . Labels denote fields  $F = F_{ion}, F_{slow}^{[\tau]}$ , and  $F_Y$ .

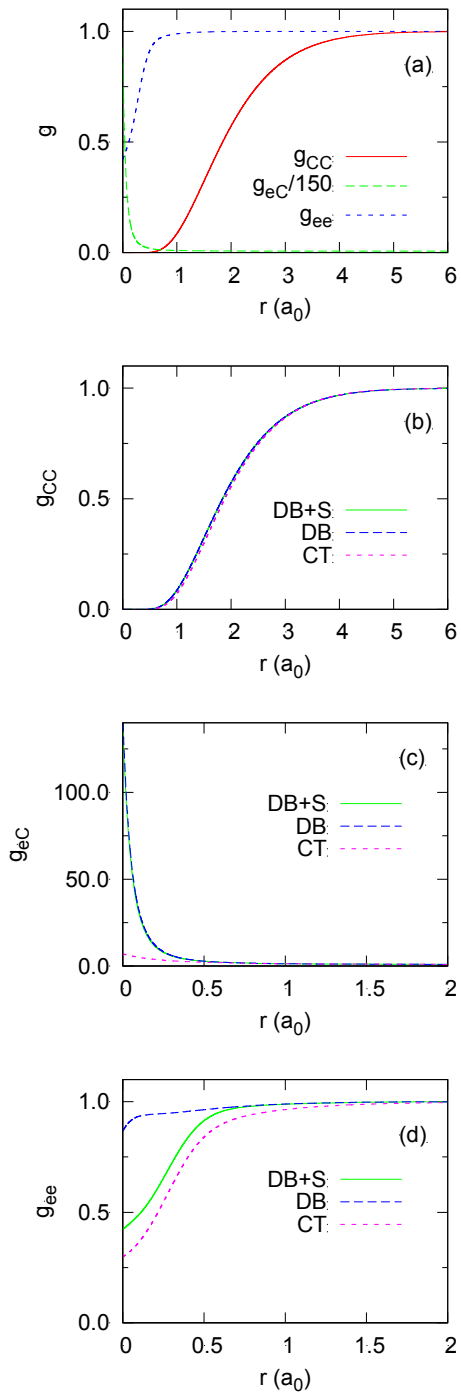


Figure 1

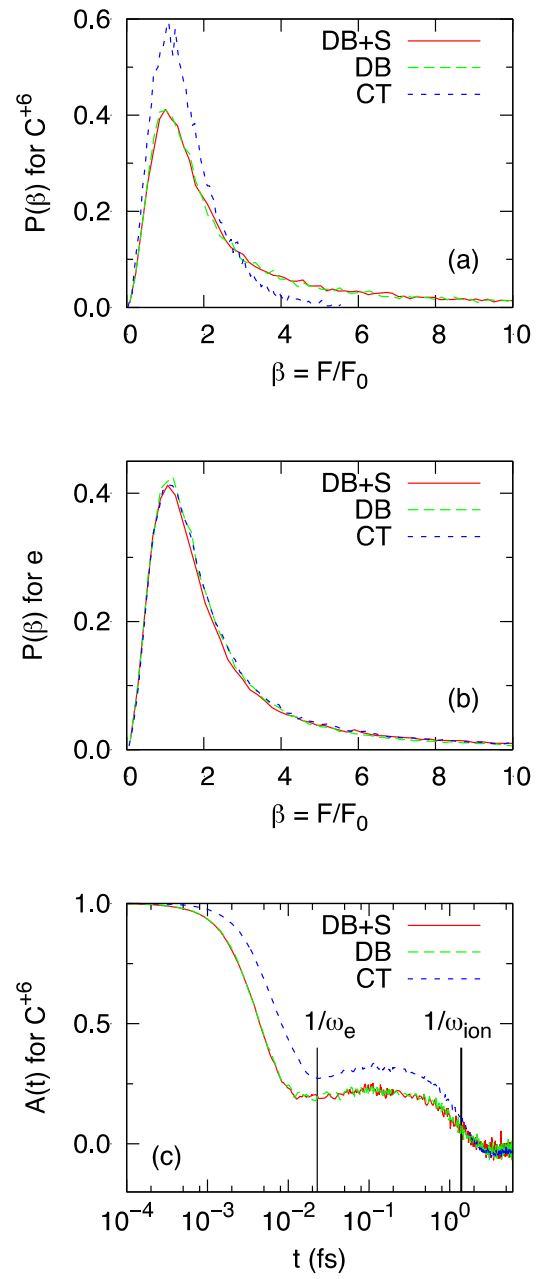


Figure 2

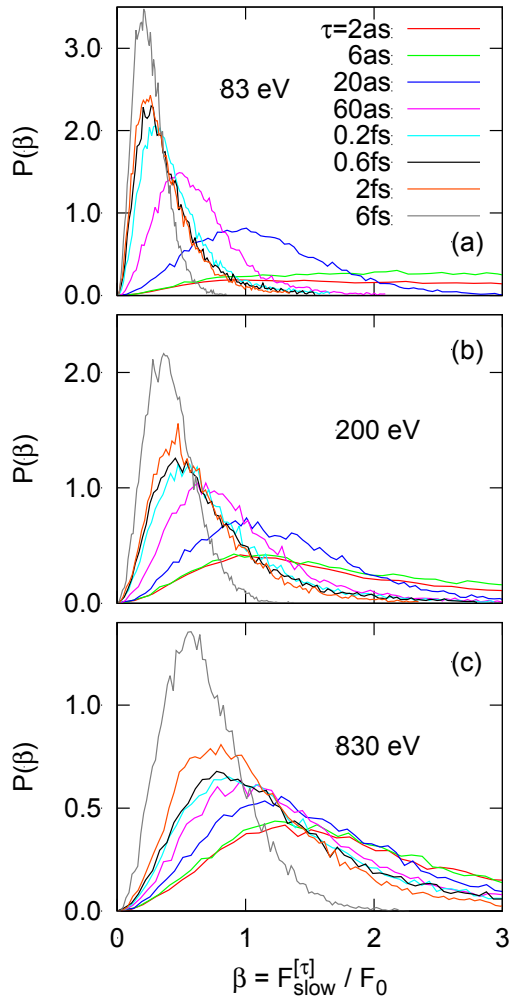


Figure 3

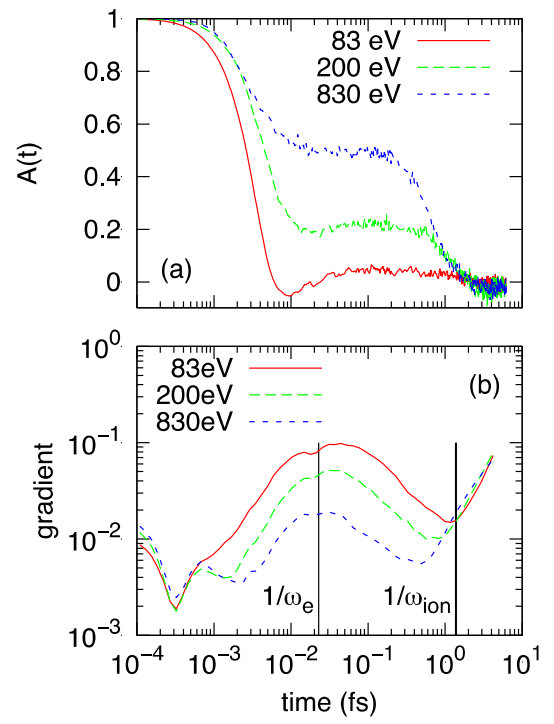


Figure 4

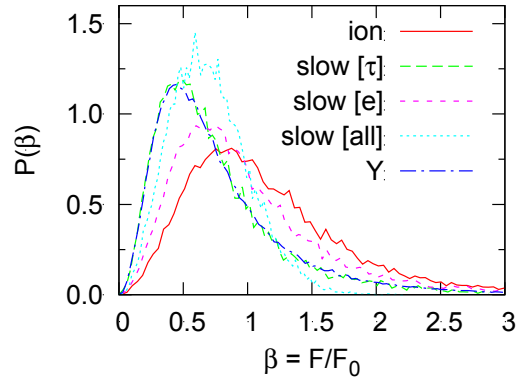


Figure 5

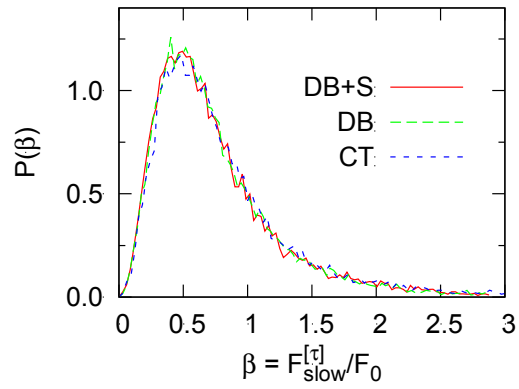


Figure 6

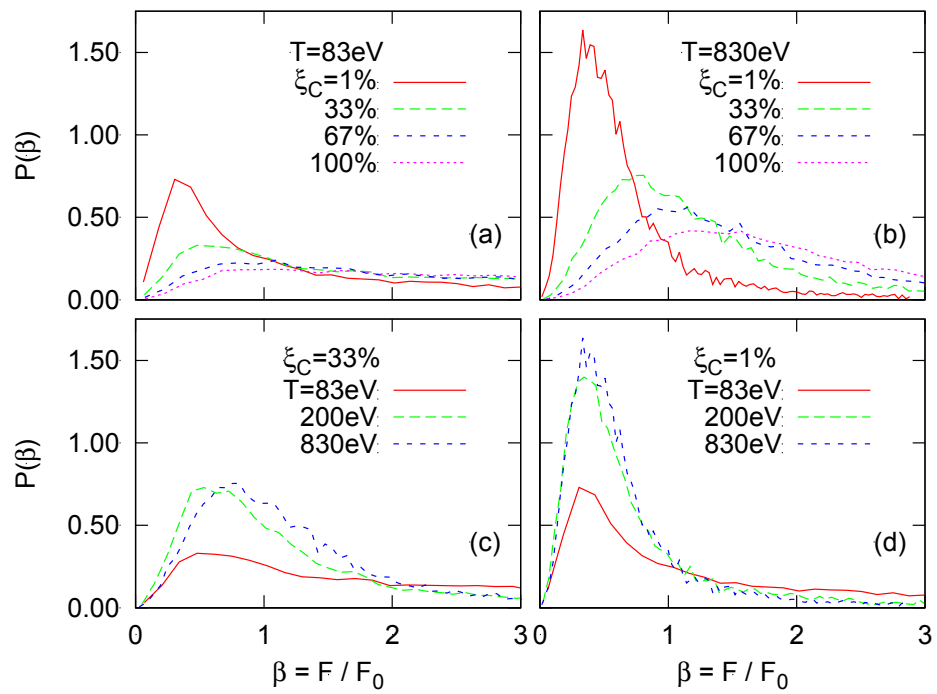


Figure 7

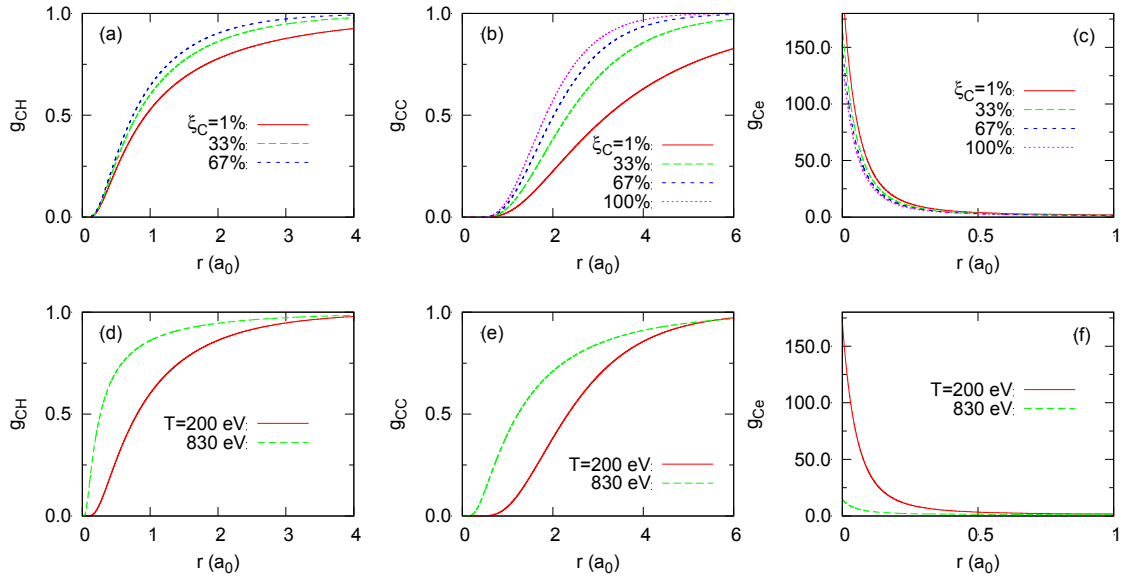


Figure 8

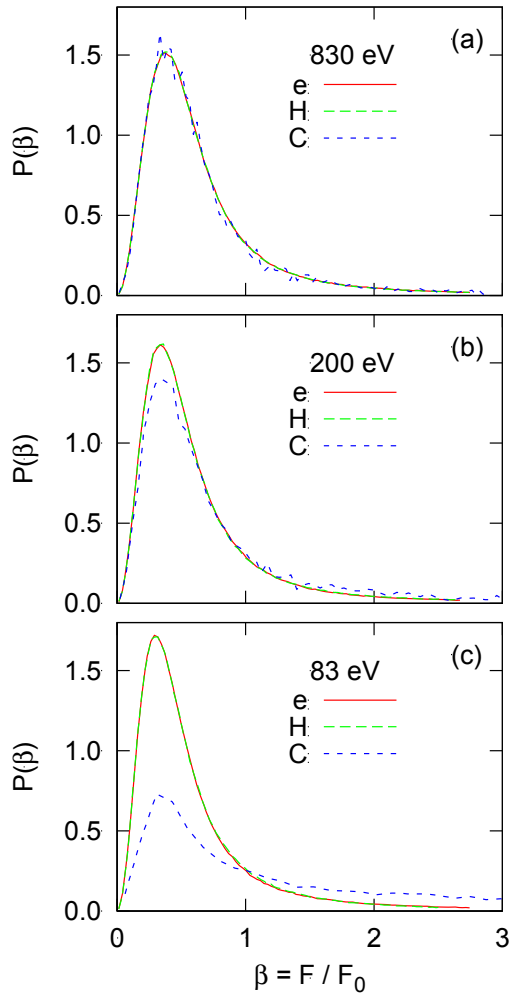


Figure 9

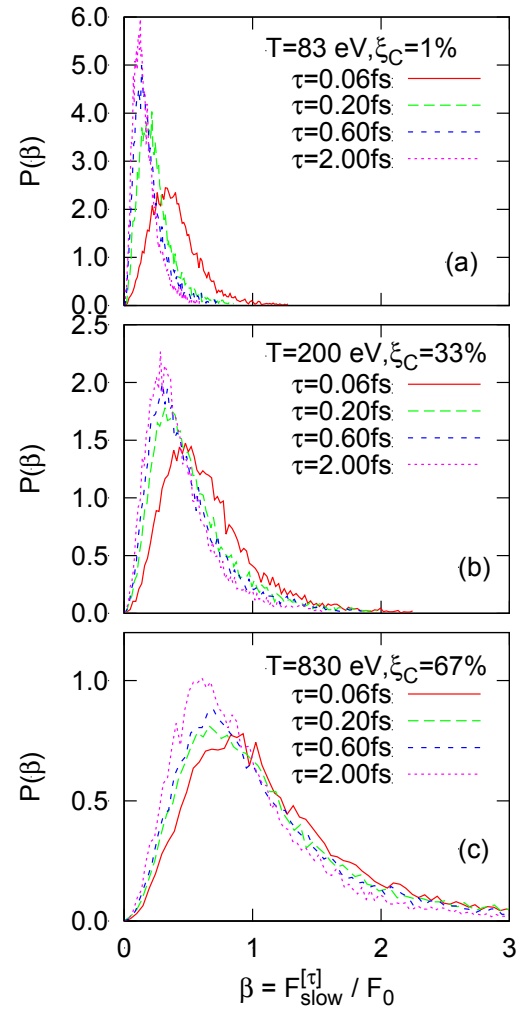


Figure 10

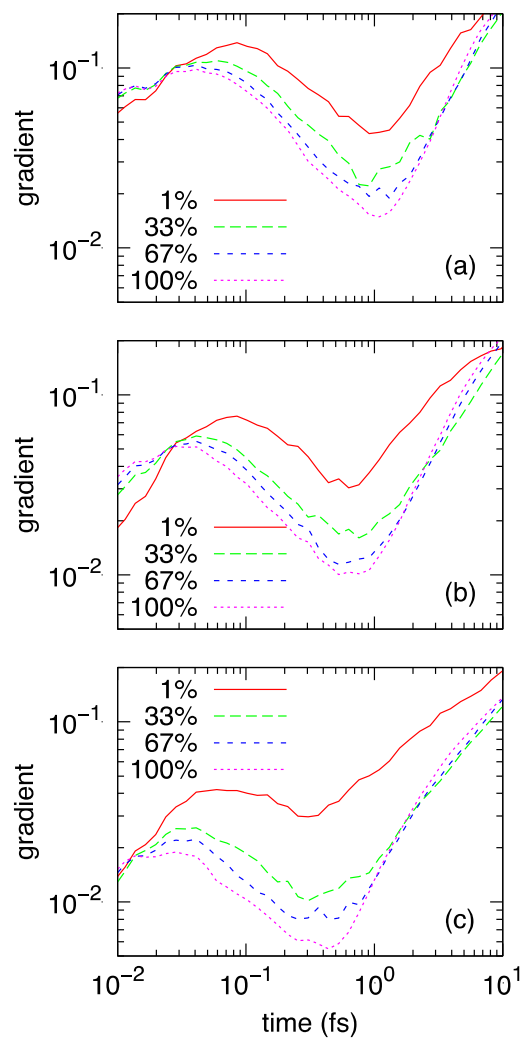


Figure 11

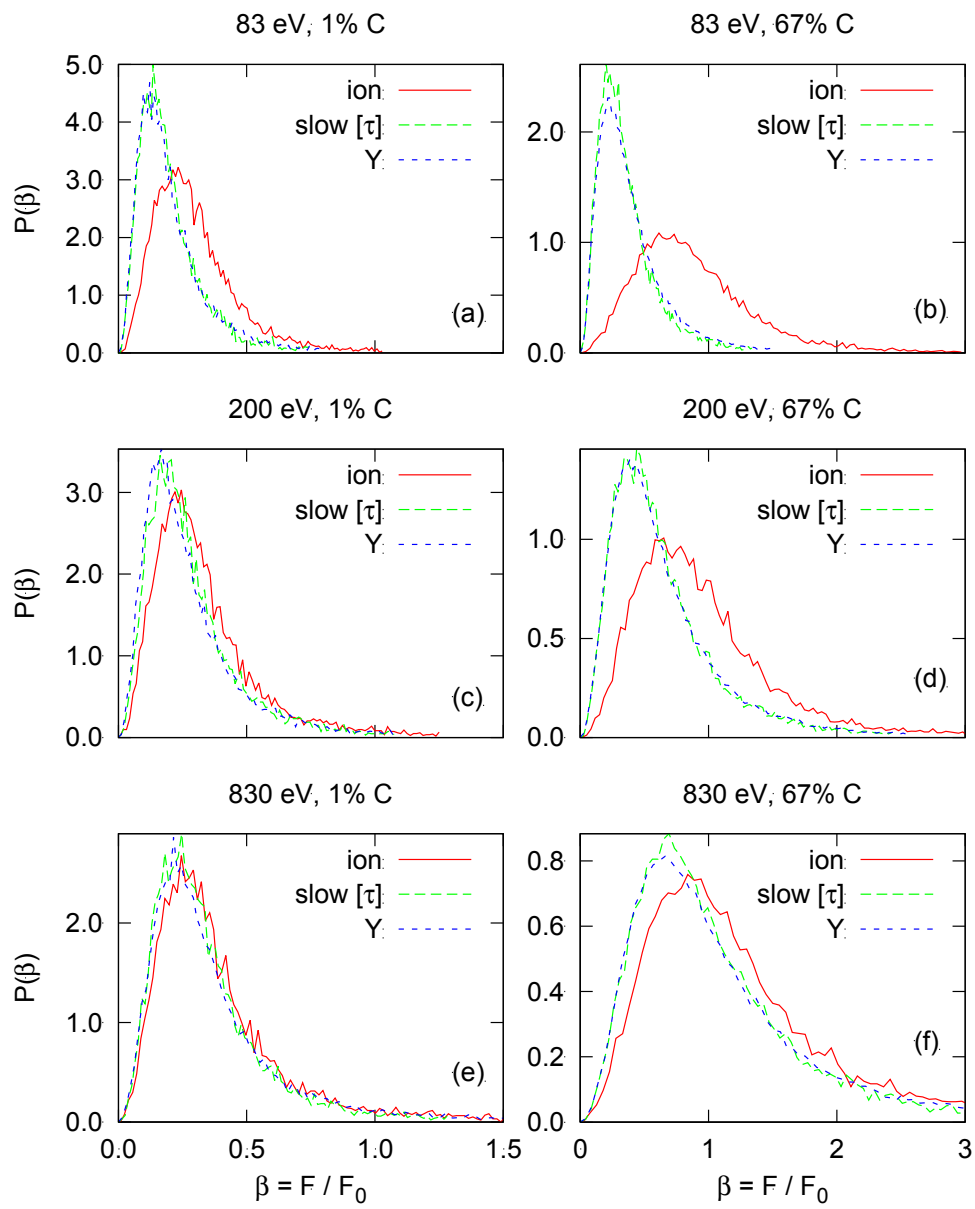


Figure 12